AGU PUBLICATIONS

Water Resources Research

RESEARCH ARTICLE
10.1002/2013WR014809

Special Section:
Patterns in Soil-Vegetation-Atmosphere Systems: Monitoring, Modelling and Data Assimilation

Moisture profiles of the upper soil layer during evaporation monitored by NMR

Steffen Merz[1], Andreas Pohlmeier[1], Jan Vanderborght[1], Dagmar van Dusschoten[2], and Harry Vereecken[1]

[1]Agrosphere (IBG-3), Institute of Bio- and Geosciences, Forschungszentrum Jülich GmbH, Jülich, Germany, [2]Plant Sciences (IBG-2), Institute of Bio- and Geosciences, Forschungszentrum Jülich GmbH, Jülich, Germany

Key Points:
- Moisture changes during evaporation investigated by NMR and MRI
- Transition from stage I to stage II evaporation
- S-shaped profiles observed with different NMR methods

Correspondence to:
S. Merz,
s.merz@fz-juelich.de

Citation:
Merz, S., A. Pohlmeier, J. Vanderborght, D. Dusschoten, and H. Vereecken (2014), Moisture profiles of the upper soil layer during evaporation monitored by NMR, *Water Resour. Res.*, *50*, 5184–5195, doi:10.1002/2013WR014809.

Received 30 SEP 2013
Accepted 6 JUN 2014
Accepted article online 10 JUN 2014
Published online 27 JUN 2014

Abstract Near-surface soil moisture profiles contain important information about the evaporation process from a bare soil. In this study, we demonstrated that such profiles could be monitored noninvasively and with high spatial resolution using Nuclear Magnetic Resonance (NMR). Soil moisture profiles were measured in a column exposed to evaporation for a period of 67 days using a stationary Magnetic Resonance Imaging (MRI) high field scanner and a unilateral NMR sensor. The column was packed with medium sand and initially saturated. Two distinct shapes of soil moisture profiles that are characteristic for stage I (evaporation rate is controlled by atmospheric demand) and stage II (evaporation rate is controlled by the porous medium) of the evaporation process were followed by both MRI and unilateral NMR. During stage I, an approximately uniform decrease of soil moisture over time was monitored, whereas during stage II, S-shaped moisture profiles developed which receded progressively into the soil column. These promising results and the specific design of the unilateral NMR system make it very well suited for determining soil moisture profiles in the field.

1. Introduction

Evaporation from bare soils is one key factor controlling water and energy exchange between the land surface and atmosphere [*Hanks et al*., 1967; *Huxman et al*., 2005; *Seager et al*., 2007]. A large body of literature describes evaporation as a two-stage process [*Coussot*, 2000; *Faure and Coussot*, 2010; *Lehmann et al*., 2008; *Scherer*, 1990; *Schlünder*, 2004; *Shokri and Or*, 2011] with an initially high and often presumed constant evaporation rate (stage I or constant rate period (CRP)) close to that of an open water surface and primarily limited by the vapor pressure deficit between surface and air and the energy available to vaporize soil water. It should be noted that in some cases, e.g., when the soil surface dries out, also transfer through the air layer above the soil may become limiting [*Schlünder*, 2004; *Shahraeeni et al*., 2012]. During stage I, evaporative demand is supplied by liquid flow from the deeper soil toward to a secondary drying front, located at the soil surface [*Yiotis et al*., 2001]. Stage I evaporation ends when the water potential at the soil surface falls below a critical threshold value. At this point of drying, capillary flow ceases and the liquid films become detached from the surface (depinning) which marks the onset of stage II or falling rate period (FRP) [*Belhamri*, 2003; *Schlünder*, 2004]. The secondary drying front recedes inside the porous medium leading to a lower evaporation rate that mainly depends on porous medium properties such as pore size distribution. In Richards' equation, only liquid flow is considered and vapor transport is neglected, which leads to an overestimated moisture content in the topmost soil layer Therefore, it is essential to take liquid water, vapor, and heat flow into consideration as demonstrated by *Saito et al*. [2006].

A couple of methods exists that estimate soil evaporation on large scales from water content distributions in the surface layer [*Abtew and Melesse*, 2013; *Viscarra Rossel et al*., 2011; *Stafford*, 1988]. Since evaporation processes are sensitive to changes in the pore system and produce steep gradients of soil moisture in the shallow layer, noninvasive methods with high spatial resolution in the vertical direction are necessary for their investigation. *Shokri et al*. [2008] and *Shokri and Sahimi* [2012] investigated drying front dynamics by means of neutron radiography and synchrotron X-ray tomography using coarse sand in a Hele-Shaw cell and a small cylinder (12 mm height and 5 mm in diameter), respectively. These methods can, however, not be applied outdoors or directly in the field.

In recent years, Nuclear Magnetic Resonance (NMR) and Magnetic Resonance Imaging (MRI) have become versatile toolkits for soil and environmental research since they allow to study processes noninvasively [*Hall*

et al., 1997; *Nestle et al*., 2002]. The main advantages are that these methods directly measure hydrogen and thus water and they provide versatile information, i.e., besides the mere water content, the local dynamics of the liquid in the pore system and the motion of tracers can also be observed [*Pohlmeier et al*., 2013]. NMR and MRI are used for a broad range of applications to study various processes and materials, e.g., drying of mortar and cement [*Faure et al*., 2012; *Valckenborg et al*., 2001; *Van der Heijden et al*., 2009], characterization of natural soils [*Haber-Pohlmeier et al*., 2010; *Jaeger et al*., 2009; *Pohlmeier et al*., 2009; *Stingaciu et al*., 2010, 2009] and rocks [*Song*, 2010], mapping of moisture content changes in porous media during drying, wetting, or drainage [*Amin et al*., 1993; *Balcom et al*., 2003; *Deurer et al*., 2002; *Faure et al*., 2011; *Sněhota et al*., 2010]. A comprehensive overview on MRI for investigation of mass transport in porous media is given by *Koptyug* [2012]. Driven by the fact that conventional MRI devices are immobile and therefore not suitable for in situ field measurements, portable NMR devices have been developed. One type is a unilateral, open U-shaped magnet, which probes a sensitive volume at some distance away from its surface [*Casanova*, 2011]. Such devices use permanent magnets instead of an electromagnet, and are therefore not as heavy as the device presented by *Paetzold et al*. [1985].

The primary objective of the present work is to investigate whether the development of a shallow dry layer during stage II of evaporation can be observed with the unilateral NMR sensor in the laboratory. Such a drying layer develops under dry soil conditions when the effective water diffusivity increases with decreasing volumetric water content due to an increasing contribution of vapor flow [*Assouline et al*., 2013; *Keulen and Hillel*, 1974; *Shokri et al*., 2008, 2010]. For this purpose, we monitored the evolution of moisture profiles in the topmost layer of a laboratory column filled with natural sand by using 3-D MRI and unilateral NMR. Classical spin echo methods may suffer from short signal lifetimes, what is mostly the case for natural soils with an increasing pore surface/volume ratio and the presence of ferromagnetic or paramagnetic elements [*Foley et al*., 1996; *Hall et al*., 1997]. Therefore, as a secondary objective, we evaluated a pure phase-encoding MRI sequence to determine water contents in soils with short signal lifetimes. As demonstrated by *Muir and Balcom* [2012, 2013], this has been proven to be an effective alternative method for fluid imaging in porous media with short signal lifetimes. We therefore compared a spin echo method to a pure phase-encoding sequence.

2. NMR/MRI Principles

If nuclei with an intrinsic magnetic dipole moment (e.g., ^{1}H) resulting from the spin angular momentum are exposed to an external magnetic field $|\boldsymbol{B}_0|$ along the z axis, the z components of their magnetic moments will align parallel or antiparallel to the direction of $|\boldsymbol{B}_0|$. For nuclei with spin = 1/2 like ^{1}H only two states exist. The energy difference between these two states is proportional to $|\boldsymbol{B}_0|$ and corresponds to a resonance or Larmor frequency $\upsilon_0 = |\boldsymbol{B_0}|\gamma/2\pi$, where γ (rad s^{-1} T^{-1}) is the gyromagnetic ratio. In thermal equilibrium, the parallel state is slightly more populated than the antiparallel state since it is energetically more favorable and Boltzmann's law describes the population ratio. Macroscopically, all individual magnetic moments sum up to the macroscopic magnetization vector, which is aligned along the z axis. If this system interacts with electromagnetic radiation matching the resonance frequency, the magnetization vector is rotated to a plane orthogonal to $|\boldsymbol{B_0}|$. This is termed the *rf-pulse*. If the pulse strength and duration are adjusted properly, all magnetization is in the x-y plane, this is a so-called 90° pulse. It should be noted that also smaller (e.g., 4°) or larger (180°) flip angle are employed when appropriate. The magnetization in the x-y plane precesses now around the z axis with the resonance frequency υ_0 and induces an observable signal (Free Induction Decay FID) which decays by two types of relaxation: (a) longitudinal or T_1 relaxation where the spins will realign along $|\boldsymbol{B_0}|$ and (b) transversal or T_2* relaxation where the spins lose their coherence due to spin-spin interactions and due to the inhomogeneity of the magnetic field. For porous media, $1/T_2$* is composed of four major partial relaxation rates:

$$1/T_2^* = 1/T_{2,bulk} + 1/T_{2,surface} + 1/T_{2,diffusion} + 1/T_{2,inhomogeneous} \quad (1)$$

where $T_{2,bulk}$ (s) is the bulk water relaxation time, $T_{2,surface}$ is the surface enhanced relaxation time at the pore walls, $T_{2,}$diffusion comprises relaxation due to diffusion in external and internal magnetic field gradients, and $T_{2,inhomogeneous}$ describes the decay due to inhomogeneity of the external magnetic field. The latter effect can be compensated for by the application of a 180° pulse after the excitation which refocuses

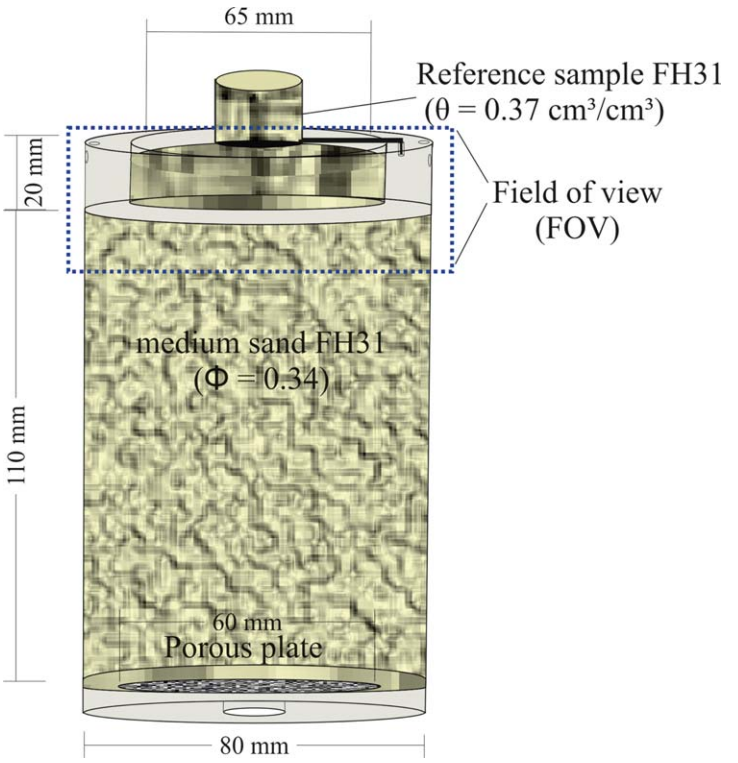

Figure 1. Schematic drawing of the sand column used for the experiments. The blue dotted line depicts the field of view (FOV = 70 mm × 100 mm). Only for this uppermost part of the column, moisture profiles were investigated by MRI.

the magnetization in the *x-y* plane and creates a so-called spin or Hahn echo at the echo time t_E after the excitation pulse [*Hahn*, 1950]. This is extended to a Carr-Purcell-Meiboom-Gill (CPMG) echo train which is the standard method for measuring T_2 relaxation what is described by the first three terms on the right-hand side of equation (1) [*Callaghan*, 1993; *Coates et al*., 1999; *Levitt*, 2001]. In bulk water with no dissolved paramagnetic compounds, motion is not restricted and therefore relaxation is very slow ($T_{bulk} \approx 3$ s), whereas in porous media, it is often controlled by fluid-solid interactions at the pore wall [*Coates et al*., 1999]. The second and the third term in equation (1) are expressed by:

$$1/T_{2,surface} = \rho_2 (S/V)_{pore} \tag{2a}$$

and

$$1/T_{2,diffusion} = D/12\ (\gamma\ G\ t_E)^2 \tag{2b}$$

where D (cm^2 s^{-1}) is the molecular diffusion coefficient, G (T m^{-1}) the strength of the internal magnetic field gradient, t_E (s) the echo time, and ρ_2 (μm s^{-1}) the surface relaxivity parameter. The surface to volume ratio of the pore $(S/V)_{pore}$ (m^{-1}) can be expressed as α/r where r (m) is the pore radius and α (–) a shape factor for pore geometry (1 = planar, 2 = cylindrical, and 3 = spherical). The initial signal amplitude is proportional to the spin or proton density and therefore to the moisture, whereas the relaxation time is a measure for the pore size, if $1/T_{2,\,diffusion}$ can be neglected. For a heterogeneous porous medium, mostly multiexponential signal decay is expected, which is calculated from CPMG echo train curves by inverse Laplace transformation. The resulting distribution of relaxation times can be related to pore characteristics, e.g., porosity, permeability, pore size distribution, and the degree of saturation in porous media [*Song et al*., 2002].

Additional switching magnetic field gradient pulses in the three Cartesian directions can spatially encode the NMR signal; this is termed as Magnetic Resonance Imaging (MRI). In spin echo imaging sequences

Table 1. Van-Genuchten-Mualem Parameters for FH 31

Bulk Density (g/cm^3)	Total Porosity (θ_s)	θ_r	K_s (cm/d)[a]	α (cm^{-1})	l	n
1.69	0.34	0.035	1300	0.0385	0.5	8.5

[a]K_s could not be determined with HYPROP©, parameter taken from *Sucre et al.* [2011].

(SEMS), one can excite multiple slices sequentially by application of a slice selective gradient during the excitation by the *rf-pulse*. The intraplane encoding proceeds further by a frequency-encoding gradient that is applied during the acquisition of the signal that is, in this case, a spin echo. The last dimension is encoded in between the excitation and spin echo detection by a so-called phase-encoding gradient. The signal, i.e., the echo is recorded in the time domain, from which the image in the real space is calculated by inverse Fourier transformation [*Gallagher et al*., 2008]. Important image parameters are field of view (FOV), matrix size, and resulting resolution, which are correlated to the pulse sequence parameters. It should be noted that also multiple echoes can employed analogous to the CPMG method in NMR relaxometry, either to accelerate image recording or to encode spatially resolved relaxometric information by the so-called multiecho multislice imaging sequence (MEMS) [*Edzes et al*., 1998].

Furthermore, many pulse sequences exist which replace the slice selection by a second phase-encoding gradient orthogonal to the other gradients. They have the advantage of higher signal intensity on expense of total measuring time. Finally, all three spatial directions can be addressed by phase-encoding gradients, which are employed in the family of single point excitation pulse sequences (SPI). A detailed description of NMR/MRI and pulse sequences can be found in *Bernstein et al.* [2004] and *McRobbie et al.* [2007], respectively.

3. Material and Methods

3.1. Porous Media

A Perspex column was packed (Figure 1) with medium sand (FH31 Quarzwerke Frechen) with a grain size distribution of 1% (>0.71 mm), 9% (0.5–0.71 mm), 33% (0.36–0.5 mm), 39% (0.25–0.36 mm), 14% (0.18–0.25 mm), and 4% (<0.18 mm). The column consisted of a cylinder with 110 mm in height and 80 mm in diameter. Due to fixing reasons in the MRI tomograph, a cylinder with 20 mm in height and 65 mm in diameter was connected to the top. The bottom was closed by a porous plate with pore size of 10–16 μm, a diameter of 60 mm, and thickness of 5 mm (Robu GmbH, Hattert/Germany). After initial saturation, the bottom was sealed, so evaporation could only take place at the column surface. Evaporation was followed over a period of 67 days. To calibrate the MRI signal on moisture, a sealed reference tube with saturated sand packing was used. All characteristic parameters of the sample are summarized in Table 1. Air temperature, relative humidity, and weight of the system were recorded hourly. The vapor pressure deficit (*vpd*) was computed as follows:

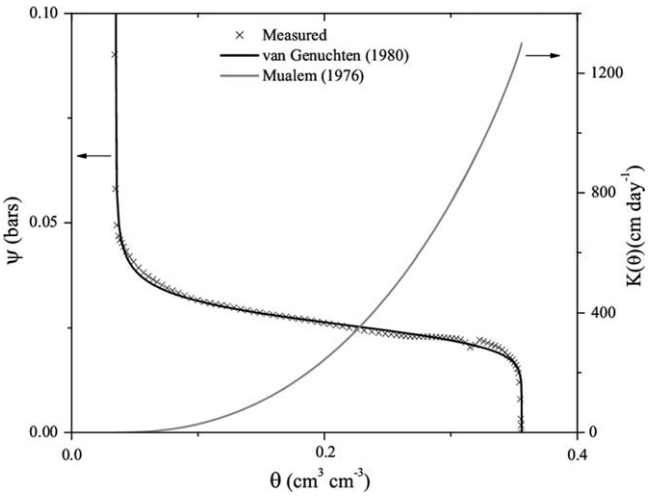

Figure 2. Water retention and hydraulic conductivity curves of the FH31 sand material. The water retention was measured using HYPROP and fitted by using the van Genuchten model with the parameters given in Table 1. The hydraulic conductivity was calculated by the approach of Mualem, and the value for the saturated conductivity was taken from *Sucre et al.* [2011].

$$\mathrm{vpd}\,[\mathrm{kPa}] = e_s(1-(\mathrm{RH}/100)) \quad (3)$$

where *RH* is the relative humidity and e_s is the saturation vapor pressure according to *Buck* [1981]:

$$e_s = F\exp(17.27T/(T+237.3)) \quad (4)$$

where $F = 0.611$ kPa and T is the temperature in °C. The temporal

Table 2. Parameters of the Spin Echo Multislice (SEMS), Single Point Imaging 3-D (SPI3D), Multiecho Multislice (MEMS), and Carr-Purcell-Meiboom-Gill (CPMG) Sequences for NMR and MRI Measurements[a]

Sequence	t_R (s)	t_E (ms)	α (°)	*NE*	*NS*	FOV (mm)	Slices	Resolution (x,z,y) (mm)	Derived Parameters	Measurement Time (min)
SEMS	10	3.04	90	1	2	70 × 100	35	0.78 × 3.1 × 0.78	*M(te)*	60
SPI3D	0.01	0.05 (t_P)	6		2	120 × 150 × 120		3.75 × 2.34 × 3.75	*M(tp)*	45
MEMS	13	4	90	128	2	70 × 100	3	0.78 × 3 × 0.78	M_o, $T_{2,eff}$	120
CPMG (4.7T)	7	2.4	90	1536	1				M_o, $T_{2,eff}$	0.05
CPMG (MOUSE)	7	0.1	90	1536	128		10	40 × 0.14 × 40	M_o	180

[a] t_R = repetition time; t_E = echo time; t_p = time after pulse; α = flip angle; *NE* = number of echoes; *NS* = number of scans; FOV = field of view; $T_{2,eff}$ = transverse (or spin-spin) relaxation time; M_0 = initial magnetization; Mobile Universal Surface Explorer (MOUSE).

evolution of the *vpd* was used as a proxy for the temporal variation of the potential evaporation of the soil column.

3.2. Hydraulic Properties

The water retention curve of the sand was measured by using the HYPROP©—Laboratory evaporation method for the determination of water retention curves and unsaturated conductivity (UMS GmbH, Munich/Germany). The bulk density and the porosity of the sample were 1.69 g cm^{-3} and 0.36 cm^3 cm^{-3}, respectively. The measured water retention curve as well as the hydraulic parameters of the sand derived from fitting the van Genuchten [*Van Genuchten*, 1980] function to the data are shown in Figure 2 and presented in Table 1. It should be noted that the saturated hydraulic conductivity K_s could not be determined for this type of sand with the HYPROP© method, and therefore, the value of *Sucre et al.* [2011] was used for computing the hydraulic conductivity function based on *Mualem* [1976].

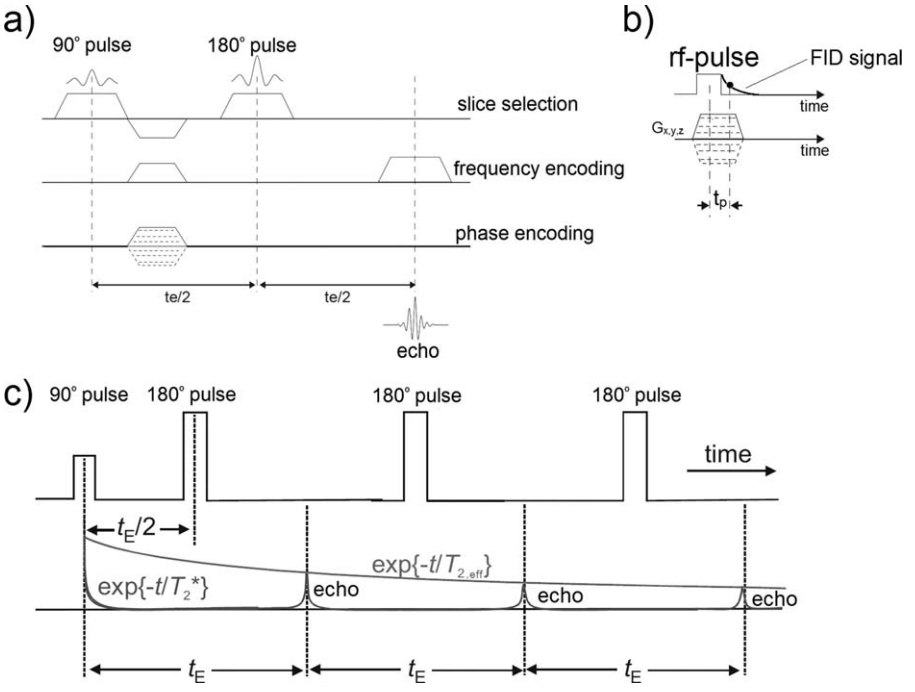

Figure 3. (a) Spin Echo Multislice (SEMS) imaging sequence. In the presence of a slice selection gradient, the spins are excited by a 90° pulse; thereafter, frequency and phase-encoding gradients ensure spatial encoding. At a certain time $t_E/2$, a 180° pulse is applied in presence of the slice selection gradient to rephrase the spins and eliminate influences of magnetic field inhomogeneity. The signal (echo) will be received after a certain time (t_E) in the presence of the frequency-encoding gradient. (b) Single Point Imaging 3-D (SPI3D). Only phase encoding in all spatial directions is used during the excitation of the complete sample volume. The signal (FID) will be recorded immediately after excitation (t_p). (c) Carr-Purcell-Meiboom-Gill (CPMG) sequence. After excitation (90° pulse) several 180° pulses (echo train) detect T_2 relaxation rate. After *Bluemich* [2005] and *Varian* [2007].

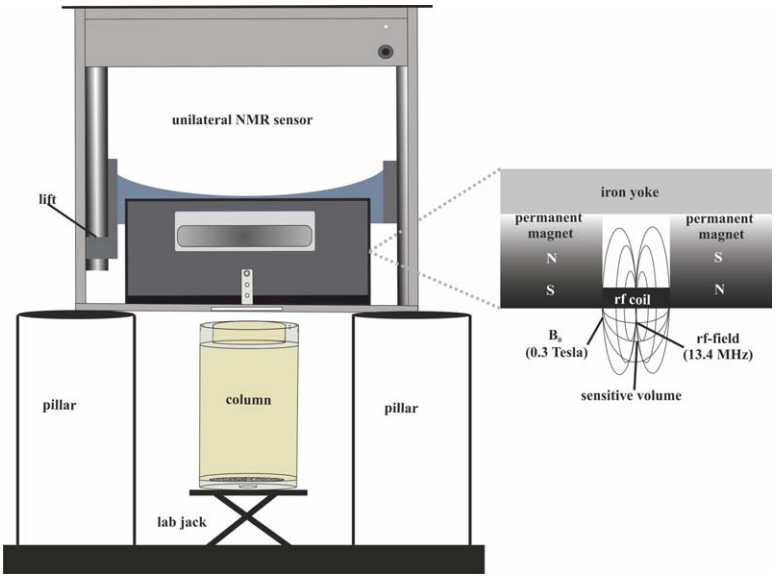

Figure 4. Mobile Universal Surface Explorer (NMR-MOUSE). The sensor is mounted on a lift, enables the sensitive volume (40 mm × 40 mm × 0.14 mm) to change the distance to or through an object, respectively. The sensor was put on the head on two pillars to investigate moisture profiles from the columns surface down to 18 mm depth.

3.3. NMR/MRI Setup

For imaging, we used a 4.7 T ($\upsilon_0 = 200$ MHz) high field vertical ultrawide bore superconducting magnet (Magnex Scientific, UK), a 300 mT/m gradient system, and a "birdcage" type quadrature *rf*-resonator with an internal diameter of 100 mm and 100 mm length, operated by a Varian console. During drying of the sample, images were recorded at certain times by two different sequences. The parameters used for MRI are listed in Table 2. Figure 3 depicts the characteristics of each sequence. For detailed information on MRI/NMR sequences, the reader is referred to *Bernstein et al*. [2004]. The position of the column inside the scanner was kept identical for all measurements, including at least 1 cm of the reference tube and 4 cm of the column inside the field of view (Figure 1). The NMR-MOUSE (Model PM-25, Magritek Ltd., Wellington/NZ) is a portable open NMR sensor, operated by a KEA^2 spectrometer (Magritek Ltd., Wellington/NZ) and processed by the Prospa software package (Magritek Ltd., Aachen/Germany). Based on the principles of "inside-out" NMR, the device is equipped with permanent magnets in U-shaped configuration generating a gradient perpendicular to the surface. The MOUSE operates at a reference frequency of 13.4 MHz with a

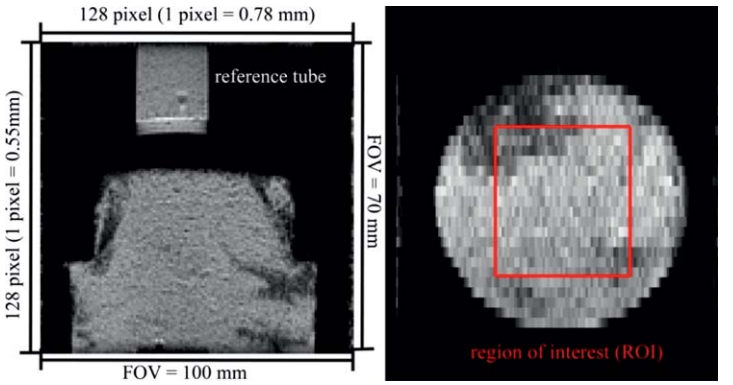

Figure 5. (left) Vertical slice of the column investigated by MRI using a SEMS sequence. (right) Horizontal slice with the determined region of interest (ROI), which is equal to the area probed by the unilateral NMR sensor.

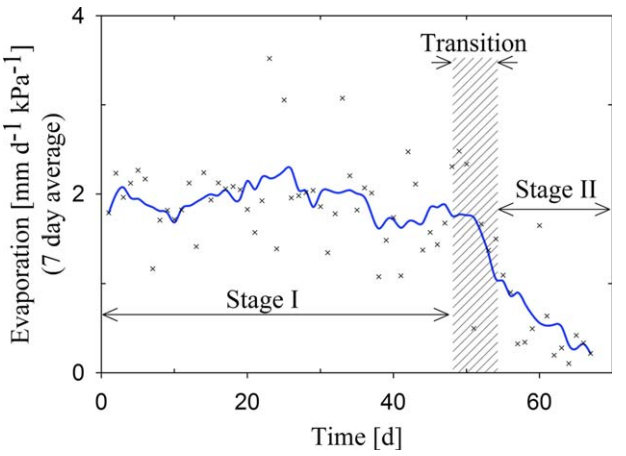

Figure 6. Evaporation rate normalized on vapor pressure deficit as an average over 7 days. The period between day 48 and 55 marks the onset of stage II evaporation.

gradient of 7.5 T/m at a distance of 25 mm from the magnet surface with a resolution (thickness of the excited volume) of 0.1 mm. The sensitive volume is excited by an *rf*-coil that is placed 5 mm above the magnet, so that the effective maximum penetration depth is 18 mm. A profile is measured by moving the magnet by a lift, where the sensitive volume is moved through the upper 18 mm of the sample. A sketch of the device is presented in Figure 4 whereas a detailed description of the system as well as the concept of single sided NMR is given in *Blumich et al*. [1998] and *Casanova* [2011]. The unilaterally measured moisture profiles were recorded using nine steps at a separation of 2 mm resulting in a maximum penetration depth of 18 mm. Table 2 lists all specific parameters for each sequence.

3.4. Moisture Profiles

MRI measurements were processed as follows:

First, the homogeneity of the sample was checked via T_2 mapping using a multiecho multislice (MEMS) sequence [*Bernstein et al*., 2004]. For each voxel, an exponential function was fitted to the echo train decay:

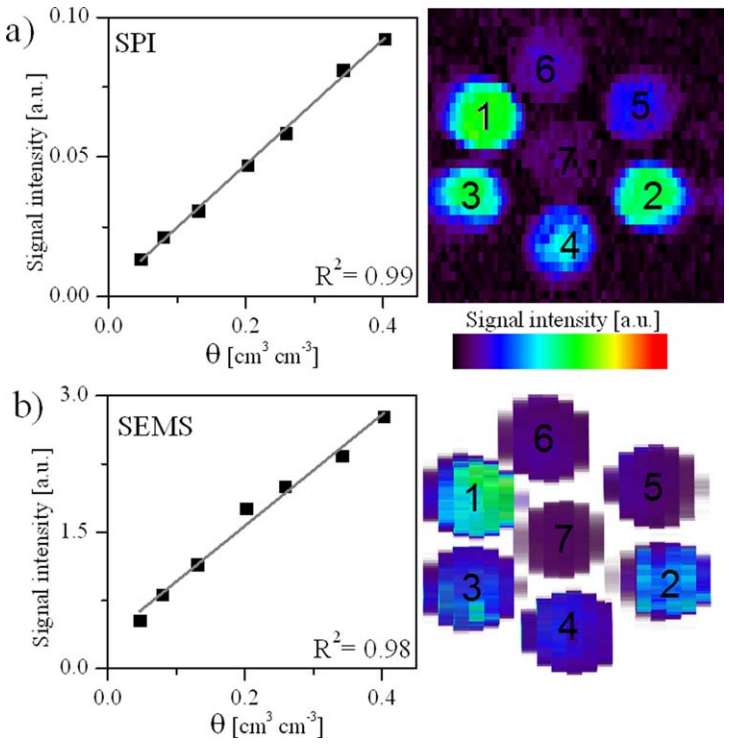

Figure 7. (left) Calibration relations between MRI signal and volumetric water content obtained with (a) SPI3D and (b) SEMS, where the gray lines are linear fits. (right) MRI cross section through the calibration phantom for (top) single point imaging and (bottom) spin echo multislice, where each pot is different in water content (θ (mm^3 mm^{-3}) 1: 0.4, 2: 0.34, 3: 0.26, 4: 0.2, 5: 0.13, 6: 0.08, 7: 0.05).

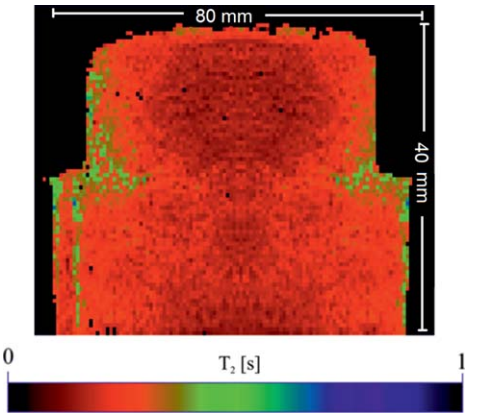

Figure 8. Vertical cross section of the saturated column. Distribution map of effective transverse relaxation times $T_{2,eff}$ obtained by fitting equation (5) to images obtained by SEMS sequence.

$$M(t) = M_0 \exp\left[-\left(NE^* t_E\right)/T_{2,eff}\right] \quad (5)$$

where $M(t)$ is the signal amplitude, M_0 the initial magnetization, NE the number of echoes, and $T_{2,eff}$ the effective T_2 relaxation time. Second, for both, SPI and SEMS, the investigated images were normalized on a saturated sample. From the normalized MRI signals and the water content of the reference sample, the moisture content for each voxel was calculated. This procedure is based on the assumption that the relation between the MRI signal and the water content is linear. To check this assumption, MRI signals of various calibration samples using the same sand with similar packing density and known water content were measured using identical parameters for SEMS and SPI3D as used for the sand column. Since the MRI signal was not homogeneous in a horizontal slice of the calibration samples, the average MRI signal of a region of interest in the calibration samples was plotted versus the gravimetric water content (Figure 5). For the unilateral sensor the following procedure was used: the obtained CPMG echo decay train was fitted by an exponential decay function (equation (5)). Since the reference sample that was used for MRI could not be measured with the unilateral NMR sensor, a water sample (with volumetric water content of 100%) was used as a reference. M_0 obtained from the soil sample was divided by M_{0ref} obtained from the water sample to determine the volumetric water content for each volume.

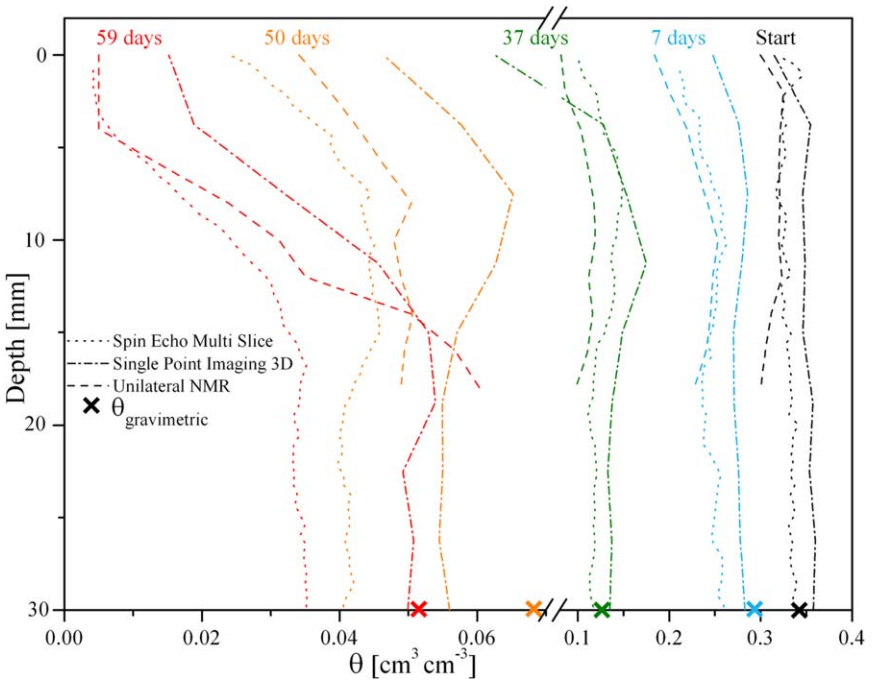

Figure 9. Moisture profiles over time monitored by SEMS, SPI3D, and the unilateral NMR for the topmost 30 mm (SEMS and SPI3D) or 18 mm (unilateral NMR) of the column (soil surface = 0). The profiles should be read from right to left starting with the saturated condition (start) on the right. The gravimetric total water contents are plotted as crosses on the abscissa.

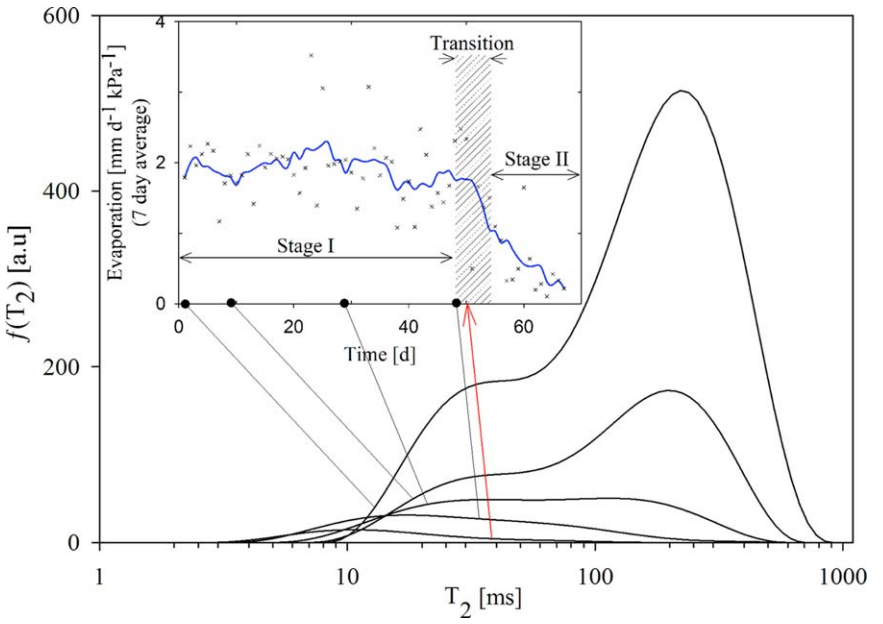

Figure 10. T_2 distribution functions for the upper 30 mm of the column over 67 days of drying. The inset shows the evaporation rate normalized on vapor pressure deficit as an average over 7 days, where the red arrow indicates the peak shift in the T_2 distribution coincided with the drop in the evaporation rate at the transition from stage I to stage II.

4. Results and Discussion

4.1. Drying Rate and Environmental Conditions

The evaporation rate normalized on the vapor pressure deficit (vpd) over 67 days is shown in Figure 6 as an average over 7 days. The evaporation rate was determined from the rate of mass loss recorded hourly by a digital balance. During stage I, the normalized evaporation rate was approximately around 2 mm d^{-1} kPa^{-1} with a corresponding total mass loss of 153.6 g. After day 52, the rate dropped to 0.75 mm d^{-1} kPa^{-1} and a continuous decrease in the normalized evaporation rate could be observed until day 67 with a corresponding mass loss of 25.6 g. During 67 days of drying, the volumetric moisture content decreased from $\theta s = 0.34$ to 0.05 cm^3 cm^{-3} after 67 days yielding an overall mass loss of 179.2 g.

4.2. MRI and Unilateral Moisture Profiles

In Figure 7, MRI images of horizontal slices through the middle of the calibration tubes obtained by SEMS and SPI are presented. Despite the fact that the sand was homogeneously packed and mixed with water, the MRI signal was not homogeneous for these tubes. The signal heterogeneities might have been caused by layering effects due to the packing, what can led either to variations in water content or in signal because of shorter T_2 times. However, these signal heterogeneities were averaged out when calculating the water content profiles. Between $\theta = 0.05$ and 0.4 cm^3 cm^{-3}, a linear relationship between signal intensity and volumetric water content was assumed to derive the moisture content from the MRI signal intensity.

Layering effects due to packing as well as cracks can influence evaporation in several ways; therefore, we checked for heterogeneities using a MEMS sequence. Figure 8 exhibits no significant heterogeneous T_2 patterns for the used column, but larger pore sizes (longer T_2) were observed near the walls where packing was less dense. The drying stages during the experiment could be linked to the shape of the vertical soil moisture profiles that were derived from MRI measurements. Figure 9 shows vertical soil moisture profiles that were monitored using MRI and the unilateral NMR sensor. During stage I, the moisture content in the upper soil layer was virtually homogeneously distributed, and the evaporation front is located at the soil surface. After reaching a critical water content at the surface (0.035 cm^3 cm^{-3} for the used column at day 50), the secondary evaporation front receded into the soil forming an increasingly thick dry surface layer. Water transport was now controlled by the vapor pressure gradient and evaporation flux proceeded via vapor transport. With increasing thickness of the dry layer, the overall evaporation rate decreased. The drop

in the normalized evaporation rate coincided with the time where a receding secondary evaporation front was observed in the moisture profiles. Onward drying, the drying rate continued to decrease and the secondary evaporation front receded deeper into the soil, with a final depth of 20 mm at day 67. The moisture content profiles obtained by SEMS (dotted lines in Figures 9) exhibited a nearly homogenous saturated upper part of the initially saturated column and are in good agreement with the gravimetrical determination. With increasing drying the profiles investigated by SEMS showed a homogenous drying behavior during stage I. The development of a steep moisture gradient in the upper 1 cm after a certain time was caused by a decrease in the capillary film which finally ceased when the critical point of drying was reached. This gradient was still detectable by SEMS after the onset of stage II but now attached to the secondary evaporation front inside the soil. Comparing the SEMS profiles to those investigated by SPI (dashed-dotted lines in Figure 9), an identical shape for both drying stages can be found. The most obvious difference between SEMS and SPI was that single point imaging exhibited higher moisture content for all profiles during both stages. These may be related to a baseline offset on the SPI measurement what led to higher moisture content. The assumption of a baseline offset was substantiated by the fact that for both SEMS and SPI, the investigated profiles were identical in shape for stage I and stage II. The constant baseline offset led to a small relative deviation at high water content and a large deviation at low water content. However, both the spin echo as well as the single point imaging sequence enabled to follow the drying process of the column down to the residual water content. For the unilateral NMR (dashed line in Figure 9) it should be noted that only the first 18 mm were monitored. The moisture profiles investigated by the sensor revealed similar homogenous drying patterns with an increasing gradient in the upper part as monitored by SEMS and SPI. Nevertheless, the investigated moisture content seems to be lower compared to SEMS and SPI. This is a consequence of the open geometry of the unilateral NMR sensor as well as the thickness of the excited slice which is only 0.14 mm.

4.3. Relaxation Analysis

Another suitable approach for following a drying process of porous media is to monitor the relaxation decay over time by using a CPMG sequence. As expected, the amplitudes of the decay curves, obtained from fitting equation (5) to the data, are directly proportional to the proton density in the measured volume and, in turn, the moisture content. The open geometry of the sensor is sensitive to environmental radiofrequency noise, where the signal to noise ratio (SNR) decreases rapidly with decreasing moisture content. The relaxation times measured with the unilateral NMR sensor are strongly controlled by diffusion of H_2O in the external 7.5 T/m gradient as described by equation (2b) [*Casanova*, 2011]. Therefore, we additionally investigated the T_2 distribution in the homogeneous magnetic field of the MRI scanner over 67 days in order to obtain information about the range of pores that remained saturated or that were partially filled with water (Figure 10). The first distribution curve reflects the condition after 4 days of drying, what in fact can be assumed as almost saturated ($\theta = 0.31$ cm^3 cm^{-3}). The distribution functions of the FH31 sand can be described as a main mode with T_2 around 250 ms with a broad shoulder at faster relaxation times (smaller pores) for the saturated conditions which broadens further at lower water contents. During the drying period, the logarithmic mean relaxation time $T_{2,av}$ shifted from 150 ms for the state at $\theta = 0.31$ cm^3 cm^{-3} after 4 days of drying to 14 ms after 67 days and the total area of the main peak decreases with time. At day 22, a slight peak shift to 160 ms was observed followed by a constant decrease in amplitude until day 52 where the peak height has decayed to almost zero. Regarding the normalized evaporation rate, the vanishing of the slow mode occurred simultaneously with a drop in the rate at the end of stage I. Now, the maximum of the distribution function is located at 20 ms and shifted further with decreasing moisture to 10 ms after 67 days. The assignment of T_2 relaxation modes to pore sizes is not straightforward, since T_2 is prone for diffusional acceleration in internal gradients [*Mitchell et al.*, 2010], especially at high magnetic fields. However, the fast mode persisted below the critical water content at the transition between stage I and stage II where continuous water films vanish. Therefore, the most likely interpretation is the assignment of the fast mode as water at the contact points between the grains and in the corners of the rough grain surface, where it is strongly retained by capillary forces. At higher water contents water in such areas will be in fast diffusive exchange with bulk water, and a differentiation from effects due to motion in internal gradients is not possible. Furthermore, bimodality can be due to chemical heterogeneity of surface sites of this natural product cannot be excluded, since *Grunewald and Knight* [2011] report on monomodal, slow relaxation in very pure quartz sand [*Grunewald and Knight*, 2011]. On the other hand, bimodal T_2 distributions of

sand packings have been reported in the literature and reproduced by numerical simulation using random walk based on pore space structure derived from analysis of μ-CT scans [see *Talabi et al*., 2009]. We conclude that the interpretation of the nature of the T_2 distribution functions in unsaturated natural sands requires further investigation, which is beyond the scope of this paper.

5. Summary and Conclusions

The aim of this study was to investigate moisture content changes in the topmost soil layer during evaporation by means of NMR imaging and a unilateral NMR sensor for assessing its later usage for field measurements. We evaporated an initially saturated sand column in the laboratory over a period of 67 days. Due to changing environmental conditions in the laboratory, we normalized the evaporation rate on the vapor pressure deficit where a transition region from stage I to stage II could precisely be determined. The shape of the soil moisture profiles, monitored by MRI using a spin echo as well as a single point imaging sequence and a unilateral NMR sensor, may also be used as an additional criterion to distinguish between stage I and stage II evaporation. The observed measurement differences between SEMS and SPI3D are small. Portable NMR measurements are feasible for $\theta > 0.03$ cm^3 cm^{-3} for the used sand and are in good agreement with the MRI profiles. Therefore, it can be concluded that each method is appropriate to study the drying stages and the onset of the development of a secondary drying front in a model soil. Finally, additional information about the shift between stage I and stage II could be obtained from high field relaxation measurements. For the saturated sand, an approximately bimodal distribution of relaxation times was observed. During stage I, the peak of the long relaxation times shifted slightly from 250 to 160 ms, decreased and finally vanished at the end of stage I. From this time, only the peak representing the fast relaxation times remained during stage II. Based on the fact that the relaxation mechanisms of transverse relaxation at high field NMR are not yet fully clear, one may assume that the rapid mode which remains during stage II evaporation is due to insulated thin water films and water in pores corners. However, this will be one subject to further investigations.

Acknowledgments
We gratefully acknowledge support by Deutsche Forschungsgesellschaft (DFG, SFB/TR 32 "Patterns in Soil-Vegetation-Atmosphere Systems: Monitoring, Modelling and Data Assimilation"). The authors thank the Editor, Associate Editor, and the three anonymous reviewers for their constructive comments which helped to significantly improve the manuscript.

References

Abtew, W., and A. Melesse (2013), *Evaporation and Evapotranspiration: Measurements and Estimations*, Springer, N. Y.
Amin, M. H. G., R. J. Chorley, K. S. Richards, B. W. Bache, L. D. Hall, and T. A. Carpenter (1993), Spatial and temporal mapping of water in soil by magnetic resonance imaging, *Hydrol. Processes*, *7*(3), 279–286.
Assouline, S., S. W. Tyler, J. S. Selker, I. Lunati, C. W. Higgins, and M. B. Parlange (2013), Evaporation from a shallow water table: Diurnal dynamics of water and heat at the surface of drying sand, *Water Resour. Res.*, *49*, 4022–4034, doi:10.1002/wrcr.20293.
Balcom, B. J., J. C. Barrita, C. Choi, S. D. Beyea, D. J. Goodyear, and T. W. Bremner (2003), Single-point magnetic resonance imaging (MRI) of cement based materials, *Mater. Struct.*, *36*(3), 166–182.
Belhamri, A. (2003), Characterization of the first falling rate period during drying of a porous material, *Drying Technol.*, *21*(7), 1235–1252.
Bernstein, M., K. King, and X. Zhou (2004), *Handbook of MRI Pulse Sequences*, Academic, Burlington, Mass.
Bluemich, B. (2005), *Essential NMR for Scientists and Engineers*, Springer, Berlin, Germany.
Blumich, B., P. Blümler, G. Eidmann, A. Guthausen, R. Haken, U. Schmitz, K. Saito, and G. Zimmer (1998), The NMR-mouse: Construction, excitation, and applications, *Magn. Reson. Imaging*, *16*(5–6), 479–484.
Buck, A. L. (1981), New equations for computing vapor pressure and enhancement factor, *J. Appl. Meteorol.*, *20*(12), 1527–1532.
Callaghan, P. T. (1993), *Principles of Nuclear Magnetic Resonance Microscopy*, Clarendon, Oxford, U. K.
Casanova, F. (2011), *Single-Sided Nmr*, Springer, Berlin Heidelberg, Germany.
Coates, G. R., L. Xiao, and M. G. Prammer (1999), *NMR Logging: Principles and Applications*, Haliburton Energy Serv., Houston, Tex.
Coussot, P. (2000), Scaling approach of the convective drying of a porous medium, *Eur. Phys. J. B*, *15*(3), 557–566.
Deurer, M., I. Vogeler, A. Khrapitchev, and D. Scotter (2002), Imaging of water flow in porous media by magnetic resonance imaging microscopy, *J. Environ. Qual.*, *31*(2), 487–493.
Edzes, H. T., D. van Dusschoten, and H. Van As (1998), Quantitative T2 imaging of plant tissues by means of multi-echo MRI microscopy, *Magn. Reson. Imaging*, *16*(2), 185–196.
Faure, P., and P. Coussot (2010), Drying of a model soil, *Phys. Rev. E*, *82*(3), 036303.
Faure, P., E. Michel, S. Sammartino, and C. Doussan (2011), Magnetic resonance imaging and relaxometry as tools to investigate water distribution in soils, *AIP Conf. Proc.*, *1330*(1), 69–72.
Faure, P., S. Caré, J. Magat, and T. Chaussadent (2012), Drying effect on cement paste porosity at early age observed by NMR methods, *Construct. Building Mater.*, *29*, 496–503.
Foley, I., S. A. Farooqui, and R. L. Kleinberg (1996), Effect of paramagnetic ions on NMR relaxation of fluids at solid surfaces, *J. Magn. Reson., Ser. A*, *123*(1), 95–104.
Gallagher, T. A., A. J. Nemeth, and L. Hacein-Bey (2008), An introduction to the Fourier transform: Relationship to MRI, *Am. J. Roentgenol.*, *190*(5), 1396–1405.
Grunewald, E., and R. Knight (2011), The effect of pore size and magnetic susceptibility on the surface NMR relaxation parameter T_2*, *Near Surf. Geophys.*, *9*(2), 169–178.
Haber-Pohlmeier, S., M. Bechtold, S. Stapf, and A. Pohlmeier (2010), Water flow monitored by tracer transport in natural porous media using magnetic resonance imaging, *Vadose Zone J.*, *9*(4), 835–845.
Hahn, E. L. (1950), Spin echoes, *Phys. Rev.*, *80*(4), 580–594.

Hall, L. D., M. H. Gao Amin, E. Dougherty, M. Sanda, J. Votrubova, K. S. Richards, R. J. Chorley, and M. Cislerova (1997), MR properties of water in saturated soils and resulting loss of MRI signal in water content detection at 2 tesla, *Geoderma*, *80*(3–4), 431–448.
Hanks, R. J., H. R. Gardner, and M. L. Faikbourn (1967), Evaporation of water from soils as influenced by drying with wind or radiation, *Soil Sci. Soc. Am. J.*, *31*(5), 593–598.
Huxman, T. E., B. P. Wilcox, D. D. Breshears, R. L. Scott, K. A. Snyder, E. E. Small, K. Hultine, W. T. Pockman, and R. B. Jackson (2005), Ecohydrological implications of woody plant encroachment, *Ecology*, *86*(2), 308–319.
Jaeger, F., S. Bowe, H. Van As, and G. E. Schaumann (2009), Evaluation of 1H NMR relaxometry for the assessment of pore-size distribution in soil samples, *Eur. J. Soil Sci.*, *60*(6), 1052–1064.
Keulen, H., and D. Hillel (1974), *A Simulation Study of the Drying-Front Phenomenon*, pp. 270–273, The State Agric. Univ., Wageningen, Netherlands.
Koptyug, I. V. (2012), MRI of mass transport in porous media: Drying and sorption processes, *Prog. Nucl. Magn. Reson. Spectrosc.*, *65*, 1–65.
Lehmann, P., S. Assouline, and D. Or (2008), Characteristic lengths affecting evaporative drying of porous media, *Phys. Rev. E*, *77*(5), 056309.
Levitt, M. H. (2001), *Spin Dynamics: Basics of Nuclear Magnetic Resonance*, John Wiley, West Sussex, England.
McRobbie, D., E. Moore, M. Graves, and M. Prince (2007), *MRI from Picture to Proton*, Cambridge Univ. Press., N. Y.
Mitchell, J., T. C. Chandrasekera, and L. F. Gladden (2010), Obtaining true transverse relaxation time distributions in high-field NMR measurements of saturated porous media: Removing the influence of internal gradients, *J. Chem. Phys.*, *132*(24), 244705.
Mualem, Y. (1976), A new model for predicting the hydraulic conductivity of unsaturated porous media, *Water Resour. Res.*, *12*(3), 513–522.
Muir, C. E., and B. J. Balcom (2012), Pure phase encode magnetic resonance imaging of fluids in porous media, in *Annual Reports on NMR Spectroscopy*, edited by A. W. Graham, pp. 81–113, Academic Press, Kidlington, Oxford.
Muir, C. E., and B. J. Balcom (2013), A comparison of magnetic resonance imaging methods for fluid content imaging in porous media, *Magn. Reson. Chem.*, *51*(6), 321–327.
Nestle, N., T. Baumann, and R. Niessner (2002), Magnetic resonance imaging in environmental science, *Environ. Sci. Technol.*, *36*(7), 154A–160A.
Paetzold, R. F., G. A. Matzkanin, and A. De Los Santos (1985), Surface soil water content measurement using pulsed nuclear magnetic resonance techniques, *Soil Sci. Soc. Am. J.*, *49*(3), 537–540.
Pohlmeier, A., S. Haber-Pohlmeier, and S. Stapf (2009), A fast field cycling nuclear magnetic resonance relaxometry study of natural soils, *Vadose Zone J.*, *8*(3), 735–742.
Pohlmeier, A., S. Haber-Pohlmeier, M. Javaux, and H. Vereecken (2013), Magnetic resonance imaging (MRI) techniques for visualization of root growth and root water uptake processes, in *Tomography and Imaging of Soil-Water-Root, SSSA Spec. Publ.*, Soil Science Society of America, Inc., Madison, Wisconsin, United States.
Saito, H., J. Šimůnek, and B. P. Mohanty (2006), Numerical analysis of coupled water, vapor, and heat transport in the vadose zone, *Vadose Zone J.*, *5*(2), 784–800.
Scherer, G. W. (1990), Theory of drying, *J. Am. Ceram. Soc.*, *73*(1), 3–14.
Schlünder, E. U. (2004), Drying of porous material during the constant and the falling rate period: A critical review of existing hypotheses, *Drying Technol.*, *22*(6), 1517–1532.
Seager, R., et al. (2007), Model projections of an imminent transition to a more arid climate in southwestern North America, *Science*, *316*(5828), 1181–1184.
Shahraeeni, E., P. Lehmann, and D. Or (2012), Coupling of evaporative fluxes from drying porous surfaces with air boundary layer: Characteristics of evaporation from discrete pores, *Water Resour. Res.*, *48*, W09525, doi:10.1029/2012WR011857.
Shokri, N., and D. Or (2011), What determines drying rates at the onset of diffusion controlled stage-2 evaporation from porous media?, *Water Resour. Res.*, *47*, W09513, doi:10.1029/2010WR010284.
Shokri, N., and M. Sahimi (2012), Structure of drying fronts in three-dimensional porous media, *Phys. Rev. E*, *85*(6), 066312.
Shokri, N., P. Lehmann, P. Vontobel, and D. Or (2008), Drying front and water content dynamics during evaporation from sand delineated by neutron radiography, *Water Resour. Res.*, *44*, W06418, doi:10.1029/2007WR006385.
Shokri, N., P. Lehmann, and D. Or (2010), Liquid-phase continuity and solute concentration dynamics during evaporation from porous media: Pore-scale processes near vaporization surface, *Phys. Rev. E*, *81*(4), 046308.
Sněhota, M., M. Císlerová, M. H. G. Amin, and L. D. Hall (2010), Tracing the entrapped air in heterogeneous soil by means of magnetic resonance imaging, *Vadose Zone J.*, *9*(2), 373–384.
Song, Y.-Q. (2010), Recent progress of nuclear magnetic resonance applications in sandstones and carbonate rocks, *Vadose Zone J.*, *9*(4), 828–834.
Song, Y.-Q., L. Venkataramanan, M. D. Hürlimann, M. Flaum, P. Frulla, and C. Straley (2002), T1-T2 correlation spectra obtained using a fast two-dimensional laplace inversion, *J. Magn. Reson.*, *154*(2), 261–268.
Stafford, J. V. (1988), Remote, non-contact and in-situ measurement of soil moisture content: A review, *J. Agric. Eng. Res.*, *41*(3), 151–172.
Stingaciu, L. R., A. Pohlmeier, P. Blümler, L. Weihermüller, D. van Dusschoten, S. Stapf, and H. Vereecken (2009), Characterization of unsaturated porous media by high-field and low-field NMR relaxometry, *Water Resour. Res.*, *45*, W08412, doi:10.1029/2008WR007459.
Stingaciu, L. R., L. Weihermüller, S. Haber-Pohlmeier, S. Stapf, H. Vereecken, and A. Pohlmeier (2010), Determination of pore size distribution and hydraulic properties using nuclear magnetic resonance relaxometry: A comparative study of laboratory methods, *Water Resour. Res.*, *46*, W11510, doi:10.1029/2009WR008686.
Sucre, O., A. Pohlmeier, A. Minière, and B. Blümich (2011), Low-field NMR logging sensor for measuring hydraulic parameters of model soils, *J. Hydrol.*, *406*(1–2), 30–38.
Talabi, O. A., S. Alsayari, M. J. Blunt, H. Dong, and X. Zhao (2009), *Predictive Pore Scale Modeling: From 3D Images to Multiphase Flow Simulations*, Soc. of Pet. Eng., Richardson, Tex.
Valckenborg, R. M. E., L. Pel, K. Hazrati, K. Kopinga, and J. Marchand (2001), Pore water distribution in mortar during drying as determined by NMR, *Mater. Struct.*, *34*(10), 599–604.
Van der Heijden, G. H. A., H. P. Huinink, L. Pel, and K. Kopinga (2009), Non-isothermal drying of fired-clay brick, an NMR study, *Chem. Eng. Sci.*, *64*(12), 3010–3018.
Van Genuchten, M. T. (1980), A closed-form equation for predicting the hydraulic conductivity of unsaturated soils, *Soil Sci. Soc. Am. J.*, *44*(5), 892–898.
Varian (2007), *VnmrJ Imaging User Guide*, edited by Everett Schreiber, Varian Inc., Palo Alto, Calif.
Viscarra Rossel, R. A., V. I. Adamchuk, K. A. Sudduth, N. J. McKenzie, and C. Lobsey (2011), Proximal soil sensing: An effective approach for soil measurements in space and time, in *Advances in Agronomy*, edited by L. S. Donald, pp. 243–291, chap. 5, Academic.
Yiotis, A. G., A. K. Stubos, A. G. Boudouvis, and Y. C. Yortsos (2001), A 2-D pore-network model of the drying of single-component liquids in porous media, *Adv. Water Resour.*, *24*(3–4), 439–460.